Top-Illuminated Avalanche Photodiodes With Cascaded Multiplication Layers for High-Speed and Wide Dynamic Range Performance

Naseem, Po-Shun Wang, Zohauddin Ahmad, Syed Hasan Parvez, Sean Yang, H.-S. Chen, Hsiang-Szu Chang, Jack Jia-Sheng Huang, and Jin-Wei Shi, *Senior Member, IEEE*

***Abstract*—In this work, a novel top-illuminated avalanche photodiode (APD) with a $In_{0.52}Al_{0.48}As$ multiplication (M-) layer is demonstrated. The cascaded M-layer design combined with the unique p-side up mesa structure allows relaxation of the fundamental trade-off between the gain-bandwidth product and the dark current. This leads to the simultaneous high-responsivity, high-speed, high-saturation-power, and low-dark current characteristics of our APDs. At around 0.9 V_{br} operation, the demonstrated device with its simple top-illuminated structure and large active window (mesa) diameter of 14 (24) μm exhibits a high responsivity (2.23 A/W), wide optical-to-electrical bandwidth (30 GHz), large gain-bandwidth product (270 GHz), low dark current (~200 nA), and a saturation current as high as 11 mA. The excellent performance of this APD structure opens up new possibilities to further enhance the sensitivity performance of receivers for coherent communications or 106 Gbit/sec PAM-4 applications.**

***Index Terms*—Avalanche photodiode, p-i-n photodiode.**

I. Introduction

The surge in popularity of over-the-top (OTT) media services and 5G mobile front-haul networks has driven up the demand for optical communication channel bandwidth. The 400 Gb/s Ethernet system which uses a pulse-amplitude modulation (PAM-4) format with a 53 Gbaud per channel has been developed to meet the requirements for faster data rates. However, when the linking distance exceeds 40 km, the limited output optical power of the electro-absorption-modulated laser (EML) transmitter [1] and the sensitivity of the p-i-n PD based receiver [2], [3] place limitations upon the optical power budget needed to maintain such a high data rate. Avalanche photodiodes (APDs) with wide optical-to-electrical (O-E) bandwidths and higher sensitivity than that of conventional PDs, have proven an effective way to alleviate the aforementioned problems on the receiver side [4], [5]. Recently, the Si/Ge based APDs have demonstrated excellent dynamic and static performance [5], [6] for > 106 Gbit/sec transmissions per lane [6]. Compared with their III-V counterparts [4], [7], [8], the Si/Ge APDs show improved dynamic performance, mainly due to the superior carrier multiplication process inside the Silicon M- layer over the III-V M-layer, which occurs in $In_{0.52}Al_{0.48}As$ [9], [10]. However, this kind of APD, in which the active Ge photo-absorption layer is usually grown on lattice-mismatched silicon substrates, interface defects become a challenge affecting the reliability under harsh operation conditions, e.g., in uncooled environments or for high optical power illuminations (~mW). In addition to the PAM-4 modulation formats, coherent communication schemes have become an alternative solution for >106 Gbit/sec transmissions [11], [12]. However, the PDs or APDs in a coherent receiver need to sustain high-speed and high-linearity performance under strong (~ mW) optical local oscillator (LO) pumping powers to ensure high sensitivity performance [13]. It has been demonstrated that with the $In_{0.52}Al_{0.48}As$ based APDs one can attain a larger signal-to-noise (S/N) ratio with a lower optical LO power compared with the traditional p-i-n PDs used for coherent applications, such as FMCW lidar [14]. Such requirements have driven the development of high-speed III-V APDs with high linearity and reliable high-power performance [15], [16], [17]. In order to ensure an increase in the bandwidth and saturation power of APDs, a gradual decrease in the thickness of both their absorber and M-layers is necessary, but this comes at the cost of lower responsivity. A relaxation in the trade-off between the bandwidth and responsivity and further improvement in the GBP has been reported for waveguide type APDs (WGAPD) using thinner absorbers [18], [19], [20], [21]. High-responsivity performance in such devices can be maintained by properly increasing the absorption length. However, the edge-coupled waveguide APD structure typically has a substantially narrower alignment tolerance than its vertically illuminated counterparts (5 vs. 25 μm) [22], [23], which is due to the smaller aperture

Manuscript received 24 May 2022; revised 25 July 2022 and 1 September 2022; accepted 4 September 2022. Date of publication 7 September 2022; date of current version 20 December 2022. This work was supported by the Ministry of Science and Technology in Taiwan under Grants 109-2221-E-008 -081-MY3 and 110-2622-E-008-022-CC2. *(Corresponding author: Jin-Wei Shi.)*

Naseem, Po-Shun Wang, Zohauddin Ahmad, Syed Hasan Parvez, and Jin-Wei Shi are with the Department of Electrical Engineering, National Central University, Taoyuan 320, Taiwan (e-mail: naseemever3@gmail.com; aaaa558513@gmail.com; zohauddin145991@st.jmi.ac.in; hasansyed695@gmail.com; jwshi@ee.ncu.edu.tw).

Sean Yang, H.-S. Chen, and Hsiang-Szu Chang are with the Source Photonics, Science-Based Industrial Park, Hsinchu 308, Taiwan (e-mail: sean.yang@sourcephotonics.com; hs.chen@sourcephotonics.com; hsiangszu.chang@sourcephotonics.com).

Jack Jia-Sheng Huang is with the Source Photonics, Science-Based Industrial Park, Hsinchu 308, Taiwan, and also with the Source Photonics, West Hills, CA 91304 USA (e-mail: jack.huang@sourcephotonics.com).

Color versions of one or more figures in this article are available at https://doi.org/10.1109/JLT.2022.3204743.

Digital Object Identifier 10.1109/JLT.2022.3204743

0733-8724 © 2022 IEEE. Personal use is permitted, but republication/redistribution requires IEEE permission.
See https://www.ieee.org/publications/rights/index.html for more information.

Authorized licensed use limited to: National Central University. Downloaded on March 27,2025 at 04:49:52 UTC from IEEE Xplore. Restrictions apply.

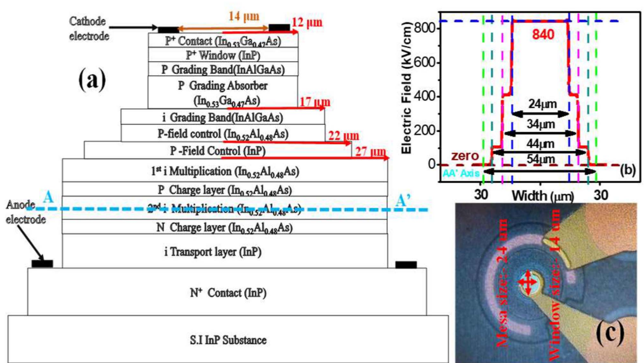

Fig. 1. (a) Conceptual cross-sectional view of Device A; (b) simulated E-field distribution in the horizontal (AA') direction; and (c) top view of the fabricated device.

size of the optical waveguides. The backside-illuminated ADP structure [4], [24] is another possibility for further enhancing the responsivity of a top-illuminated structure because of the double pass of the incident optical signal through the topmost contact metal, which serves as a reflector. However, the flip-chip bonding package for backside illumination usually induces parasitic capacitance, which degrades the net O-E bandwidth of the PD [25]. In this work, we demonstrate a novel $In_{0.52}Al_{0.48}As$-based top-illuminated APD design. The incorporation of a cascaded M-layer [14], [26] in this device enables it to attain a high multiplication gain, compensating for its low unity-gain responsivity (0.3 A/W). At around 0.9 V_{br} operation, this device, with its large active window (mesa) with a diameter of 14 (24) μm for easy optical alignment, exhibits a wide O-E bandwidth (30 GHz), high responsivity (2.23 A/W, gain $M_G = 7.43$), large gain-bandwidth product (270 GHz), low dark current ($\sim$200 nA), and a saturation current as high as 11 mA. The excellent performance of our demonstrated APD structure opens up new possibilities to further enhance the sensitivity performance of receivers for coherent or PAM-4 optical communications.

II. Device Structure Design and Fabrication

Fig. 1(a) shows a conceptual cross-sectional view of the structure of the demonstrated device. Note that these figures are not drawn to scale. The epi-layer structure, from top to bottom, is composed of a p++$-In_{0.53}Ga_{0.47}As$ contact layer, p++$-$InP window layer, p-type partially depleted $In_{0.53}Ga_{0.47}As$ absorber, composite p-type $In_{0.52}Al_{0.48}As$/InP charge layers, dual intrinsic $In_{0.52}Al_{0.48}As$ multiplication (M-) layer, n-type $In_{0.52}Al_{0.48}As$ charge layer, thick InP collector (transport) layer, and bottommost InP n+ contact layer, grown on a semi-insulating (S.I.) InP substrate. To meet the APD bandwidth requirements, we further reduced the absorber and total M-layer thicknesses, as described in our previous work [16]. In the traditional APD structure, this bandwidth enhancement usually comes at the cost of a degradation in the responsivity and increase in the dark current [4], [8]. Here, a dual M-layer structure is adopted to release the trade-off between the speed, dark current, and responsivity [14], [26]. The M-layer is divided into two parts, specified as the 1st and 2nd M-layer in Fig. 1(a), with an additional control layer between. Such a design introduces a stepped electric field profile with most of the avalanche process confined to the extremely thin 2nd M-layer, which has the highest E-field across the whole epi-structure, so that a short avalanche delay time, high GBP, and low excess noise can be expected. Furthermore, as compared to directly downscaling of a single M-layer as in the traditional APD to the same thickness as our 2nd M-layer, the addition of the 1st M-layer in our design can effectively suppress the tunneling leakage process and provide a lower overall dark current. For more details, please refer to our previous work [14], [26]. A composite charge layer ($In_{0.52}Al_{0.48}As$/InP) design is adopted to ensure that the electric field at the side wall of the bottom (2nd) M-layer becomes exactly zero and the phenomenon of edge breakdown is suppressed [16]. Selective chemical wet etching is used between these two layers to precisely etch away the charge layer above the M-layers to obtain a zero E-field at the edge. The simulated E-field distribution in such a structure will be discussed later and is illustrated in Fig. 1(b).

In addition,[1] the insertion of an InP collector (transport) layer below the M-layer releases the burden imposed on the RC-limited bandwidth, allowing for a further enlargement of the APD's active diameter for a larger alignment tolerance in the APD package. The InP layer provides a larger overshoot electron drift-velocity than can be achieved using a $In_{0.52}Al_{0.48}As$ based collector layer [27], which can further relax the trade-off between the device active area and its RC-limited bandwidth. Moreover, in comparison to the inverted p-side down APD structure [4], further improvement in the output saturation power of our p-side up structure can be expected. This is made possible by the fact that the bottom-most InP substrate is close to the 2nd M-layer having the highest E-field which allows for efficient device heat sinking. Fig. 1(a) shows the quintuple mesa structure used in our devices. As can be seen in the figure, three kinds of devices (A to C) with three different first p-mesa diameters (24, 26, and 30 μm), were fabricated in order to precisely extract the internal carrier transit time in our demonstrated APD epi-layer structure [16], which will be discussed in more detail later. During device fabrication, a 24 μm diameter 1st mesa was etched through the p-type absorber layer followed by selective wet etching to form a 34 μm diameter 2nd mesa which stopped at the InP field control (charge) layer. A thin 3rd mesa with a diameter of 44 μm was formed by the InP charge layer above the first M-layer. Finally, we etched through the M-regions down to the N^+ contact layer to obtain a 4th mesa with a diameter of 54 μm. For a detailed view of the mesa structure, please refer to Fig. 1(a). A simulation of the electric-(E-) field distribution within the device was carried out using the Silvaco Technology Computer Aided Design (TCAD) tools[1]. An undesired avalanche breakdown process can be avoided by an appropriate selection of the doping density in the charge layers so that the E-field in the absorption and collector layers is much less than their corresponding critical fields, that is 150 kV/cm for $In_{0.53}Ga_{0.47}As$ and 500 kV/cm for InP, respectively [28]. The measured values of V_{br} and V_{pt} will be discussed in detail later.

[1]Silvaco, 2811 Mission College Boulevard, 6th floor, Santa Clara, CA 95054.

Authorized licensed use limited to: National Central University. Downloaded on March 27,2025 at 04:49:52 UTC from IEEE Xplore. Restrictions apply.

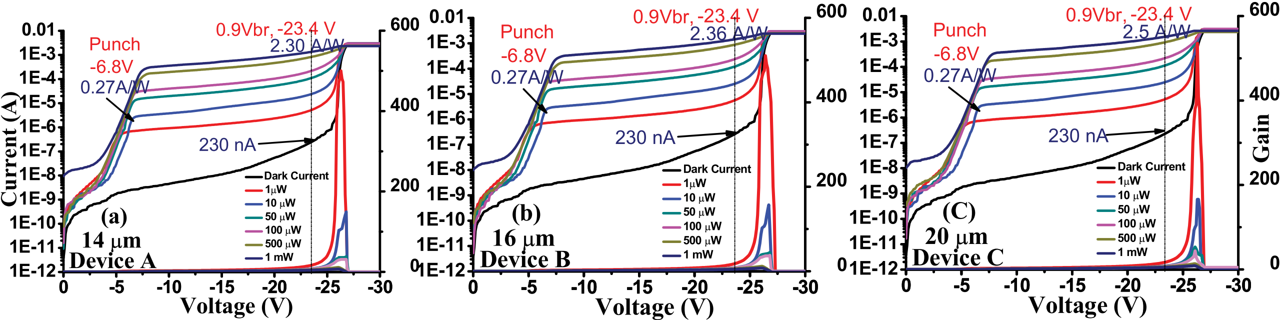

Fig. 2. Measured dark current, photocurrent, and operation gain versus bias voltage under different optical pumping powers at the 1.31 μm wavelength for all three APDs with different active window sizes: (a) Device A, (b) Device B and (c) Device C.

The measured I-V curves are shown in Fig. 2. The calculated E-field in the bottom M-layer in the horizontal direction (AA') at the breakdown voltage (V_{br}: -26 V) is depicted in Fig. 1(b). We can clearly see that the horizontal E-field (840 kV/cm) in the bottom M-layer is well confined within the range of the top p-mesa in the 24 μm diameter device, and it can be greatly reduced to zero at the edge of bottommost M-layer, as discussed above. Fig. 1(c) shows a top view of the fabricated device with a 24 (14) μm diameter active mesa (window).

III. Device Measurement Results

The bias-dependent dark current, photocurrent, and operation gain of devices A to C, measured under various optical pumping powers at the optical wavelength of 1.31 μm, are shown in Fig. 2(a) through (c), respectively. The measured punch through voltage (V_{pt}) and breakdown voltage (V_{br}) at around -6.8 and -26 V can be seen. The measured V_{pt} here is consistent with the C-V measurement result, which indicates full depletion of our epi-layer structure when the reverse bias is over -6.5 V. The demonstrated devices exhibited a much lower dark current around 200 nA at 0.9 V_{br} than those reported for APDs with close 3 dB O-E bandwidth values for 106 Gbit/sec applications (> 1 μA at 0.9 Vbr) [6], [8], [20]. This can be attributed to the unique cascaded M-layer design and the elimination of edge breakdown achieved by the addition to the design of the special composite charge layer, as illustrated in Fig. 1. Under a 1.31 μm wavelength and low optical illumination power values ($\sim$10 (1) μW) at 0.9 V_{br}, the measured responsivity is around 2.3 (5), 2.36 (5.1) and 2.5 (5.3) A/W for the three devices A to C, respectively. The corresponding gain under an optical power of 10 μW is 7.67, 7.86, 8.33 for devices A to C, respectively. Here, the chosen unity-gain responsivity of our fabricated device is around 0.3 A/W, which is close to the responsivity (0.27 A/W) measured at around V_{pt}, assuming nearly zero optical coupling loss with a single pass of injected light into the absorption layer [29]. The slight improvement of device responsivity with the increase of window size can be attributed to the minimization of the coupling loss between the launched optical signal, which has a spot size around 2 μm in diameter through the lensed fiber tip, and the active optical windows of the devices. For reference, the figures also show the gain versus bias voltage for different optical powers 1 to 1000 μW. When the reverse bias voltage is greater than the V_{br}, all of the measured operation gains are significantly reduced due to a massive increase in the dark current, which occupies the majority of the measured total current (i.e., summation of the photocurrent and the dark current). Furthermore, we can clearly see a gradual decrease in the maximum operation gain as the pumping power increases. This phenomenon is explained by the space charge screening (SCS) effect, which is caused by the photo-generation of holes in the $In_{0.53}Ga_{0.47}As$ absorption layer which lowers the net E-field and multiplication gain in the M-layer [29]. Nevertheless, for the same values of optical pumping power (-20 dBm), our demonstrated APD exhibited a maximum gain more than three times larger (45 vs. 14 A/W [6]) than the gain and responsivity reported for its III-V [7] and Si-Ge [6] counterparts. This can be attributed to the lower dark current and more pronounced avalanche process facilitated by our dual M-layer design.

Figs. 3 and 4 show the bias dependent O-E frequency responses of the three devices, A to C, measured at the wavelength of 1.55 μm under low (0.01 mW) and high (1 mW) optical powers, respectively. The corresponding responsivity of each trace is specified on these two figures. Although the optical wavelength chosen for dynamic measurement here was slightly different from that used for static measurements (1.55 vs. 1.31 μm), as shown in Fig. 2, the changes of operation gain and responsivity of the demonstrated APD structure across such optical wavelengths (1.31 to 1.55 μm) is very small according to our measurement results. Moreover, our device may exhibit faster speed performance under 1.31 wavelength operation than that under 1.55 μm due to the stronger photo-absorption process in the topmost p-type absorber, which would lead to a less pronounced hole transport effect across the active absorption region [30]. Overall, the bandwidth numbers quoted here for our devices should not be overestimated for practical applications. The fitted bandwidth curves green in colour at around 0.9 V_{br} (-23 V) are shown in Fig. 3. It can be clearly seen that device A exhibits a 30 GHz 3-dB bandwidth with a 2.23 A/W responsivity under a gain of $M_G = 7.43$ at a bias voltage of approximately 0.9 V_{br} (-23 V) and low optical power excitation. The speed and responsivity demonstrated by this APD with its simple top-illuminated structure is superior even to that of its back-side illuminated III-V counterpart with the same 14μm window size,

Authorized licensed use limited to: National Central University. Downloaded on March 27,2025 at 04:49:52 UTC from IEEE Xplore. Restrictions apply.

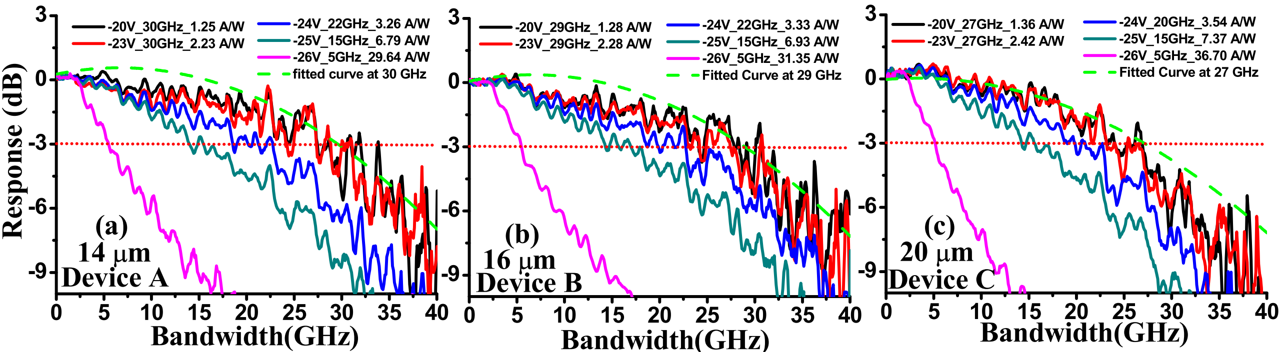

Fig. 3. Measured bias dependent O-E frequency responses of Devices A to C under a low 10 μW optical pumping power at the 1.55 μm wavelength.

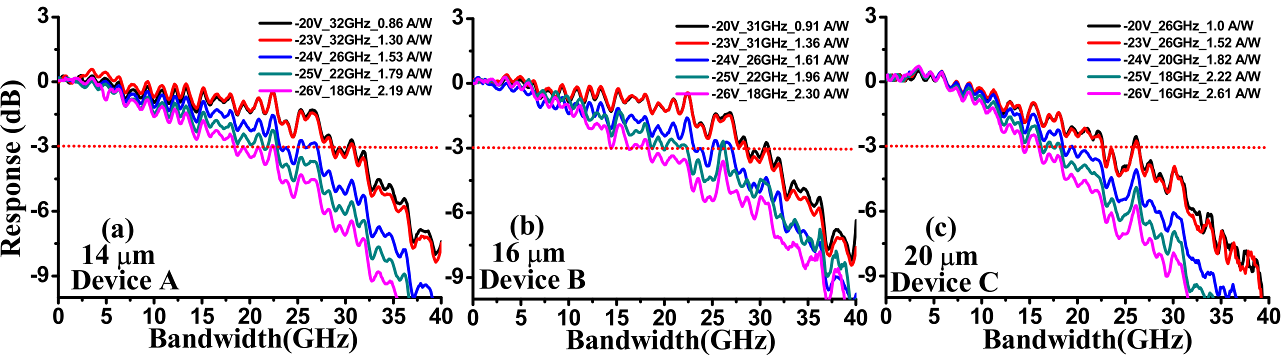

Fig. 4. Measured bias dependent O-E frequency responses of Devices A to C under a low 1 mW optical pumping power at the 1.55 μm wavelength.

TABLE I
PERFORMANCE COMPARISON OF DIFFERENT TYPES OF APDS

Parameter	NTT	SiFotonics Technology	Albis (APD20E1)	This work
Reference	8	6	31	
Type	Backside-illuminated	Topside-illuminated (Reflector on Backside)	Topside-illuminated	Topside-illuminated
Mesa Size	14 μm	20 μm	window size 14 μm	24 μm (window size 14 μm)
Dark Current (0.9 V_{br})	2 μA	0.9 μA	-	200 nA
Responsivity	1.95 A/W	3.53 (6.5) A/W	4 A/W	2.23 (3.3) A/W
Bandwidth	28 GHz	28 (22) GHz	20 GHz	30 (22) GHz
Optical Saturation Power (Damage Threshold)	-	0 dBm	5 dBm	8.8 dBm

which has a 28 GHz bandwidth and 1.95 A/W responsivity, [7], [8]. Table I shows the benchmark values reported for the high-performance APDs used for 28 or 56 Gbaud applications [8], [6]. As can be seen, the measured responsivity of our device is less (3.3 vs. 6.5 A/W) than that of its top-illuminated Si-Ge counterpart with backside reflectors under the same operation speed (~22 GHz at 0.95 V_{br}). These results suggest that, in order to compete with Si-Ge APDs, whose Silicon based M-layers are intrinsically superior to those of most III-V materials, it is preferable to combine our $In_{0.52}Al_{0.48}As$ based dual M-layer design with a back-side illuminated structure [7], [8], back-side reflectors [6], [9], or waveguide structures [20], [21]. As previously discussed, in addition to the bandwidth and the responsivity, the high-power performance of an APD is also an important parameter for >106 Gbit/sec coherent communications between data centers. As shown in Fig. 4, under 1 mW optical power illumination, devices A, B and C can maintain a 3-dB bandwidth at 0.9 V_{br} of approximately 30, 29 and 27 GHz respectively. Furthermore, in contrast to the measured traces in Fig. 3, the speed performance here is not as sensitive to the applied bias voltage. Such consistent high-speed performance indicates the good linearity and excellent high-power performance of our demonstrated device. This phenomenon, as illustrated in Fig. 2, can be attributed to the significant decrease in the value of the operation gain and the far lower sensitivity to the reverse bias voltage during high-power operation. The delay time induced by the avalanche gain, which is an APD's primary bandwidth limiting factor at high-bias operation, is minimized,

Authorized licensed use limited to: National Central University. Downloaded on March 27,2025 at 04:49:52 UTC from IEEE Xplore. Restrictions apply.

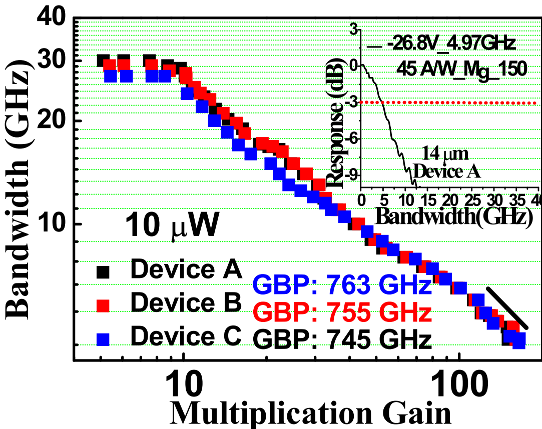

Fig. 5. Measured 3-dB O-E bandwidth versus multiplication gain. Inset shows the measured O-E frequency response of the demonstrated APD at a low optical pumping power (10 μW) and near maximum gain (150) operation.

leading to the observed invariance in the 3-dB O-E bandwidth [32]. Fig. 5 depicts the gain bandwidth products (GBP) of devices A to C measured at a low (10 μW) optical pumping power. As can be seen, very high GBPs of 745755 and 763 GHz can be achieved for Devices A, B and C, respectively, with a 0.30 A/W unity-gain responsivity in the high-gain regime. The obtained GBP values (~750 GHz) are much larger than those reported for high-speed $In_{0.52}Al_{0.48}As$ based APDs (~320 GHz) [4], [33] under the same extremely high-gain operating conditions.

The inset to Fig. 5 depicts the corresponding measured O-E frequency response, which has a 3-dB bandwidth at around 5 GHz, under low input power (10 μW), high gain (150) operation for Device A. The results suggest that our dual M-layer design can further improve the maximum intrinsic speed performance of the APD without seriously increasing the tunneling leakage current, as shown in Fig. 2. However, in practical applications, the APD is never operated in such a high gain region due to the high excess noise. For the $In_{0.52}Al_{0.48}As$ based APD, the operation point for optimized sensitivity usually happens at a gain of around 10, which corresponds to 270 GHz GBP in our device. The corresponding bias voltage and bandwidth are -23.6 V and 27 GHz, respectively. Such an improvement in the static and dynamic APD performance can be attributed to the fact that the effective multiplication layer is thinner than in typical APDs with their uniformly thick M-layer. As a result, localization of the 2nd M-layer which has a higher E-field than 1st M-layer for impact ionization decreases the possibility of avalanching in the entire M-layer and improves the GBP [33]. Note that, rather than directly reducing the thickness of the M-layer, our design uses an additional 1st M-layer to provide a lower tunneling leakage current, illustrated in Fig. 1. In addition, because both M-layers contribute to the multiplication gain, the overall gain in our layered structure becomes larger. The excellent GBP performance indicates that our composite charge layer design effectively suppresses the edge breakdown, allowing the avalanche process to be concentrated within the small volume of the M-layer below the active mesa, as illustrated in Fig. 1.

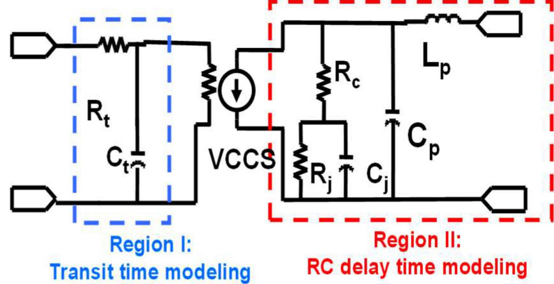

Fig. 6. Equivalent-circuit-model. VCCS: Voltage controlled current source.

TABLE II
VALUES OF THE CIRCUIT ELEMENTS

	Physical Meaning	Devices A	B	C
C_j	Junction Capacitance (fF)	84	96	130
R_c	Junction Resistance (kΩ)	12	12	12
R_s	Contact Resistance (Ω)	21	21	21
C_p	Parasitic Capacitance (fF)	77	90	120
L_p	Parasitic Inductance (pH)	21.1	21.1	40

The overall O-E 3-dB bandwidth ($f_{3\mathrm{dB}}$) of the APDs is determined by the carrier transport time $1/f_t$ and the RC time constant $\frac{1}{f_{RC}}$. The bandwidth limiting factor of our demonstrated device is calculated using the following equation adapted from [29]:

$$\frac{1}{f_{3dB}^2} = \frac{1}{f_{RC}^2} + \frac{1}{f_t^2} = (2\pi RC)^2 + \frac{1}{f_t^2} \quad (1)$$

where R is the sum of the parasitic and the load resistance (50 Ω) and C is the total capacitance. Here, the equivalent circuit modeling technique is applied to extract the RC-limited bandwidths fitted to the measured scattering parameters of the microwave reflection coefficients (S_{22}) [29]. Fig. 6 shows the equivalent circuit model that was used to fit the device's S_{22} parameters. Table II shows the fitted values for each circuit element. The fitted and measured frequency responses for devices A to C that correspond to the S_{22} parameters are shown in the Smith charts in Fig. 7(a) to (c). There is obviously a in the Smith charts in Fig. 7(a) to (c). There is obviously a close match between the simulation and the measurement results. During the modeling process, the two artificial circuit elements, R_T and C_T, are removed in order to extract the extrinsic f_{RC} of the APD. This is because they are used to mimic the low-pass frequency response of the internal carrier transit time [24], [25]. By carefully selecting the values of R_T and C_T to fit the measured O-E frequency response, it is possible to determine the internal transit time limited frequency responses of our device.

Fig. 8(a) to (c) show the measured O-E, fitted O-E, extracted RC-limited, and transit time limited frequency responses under 23 V, for devices A to C, respectively. As can be seen, the RC-limited bandwidths of devices A and B are not far from the 43 GHz transit time-limited bandwidth. This suggests that the total thickness of the depletion layers in the 24 and 26 μm active mesa diameter devices is nearly optimal for balancing the internal carrier transit time and external RC-limited bandwidth. Equation (1) can also be used to calculate the internal

Authorized licensed use limited to: National Central University. Downloaded on March 27,2025 at 04:49:52 UTC from IEEE Xplore. Restrictions apply.

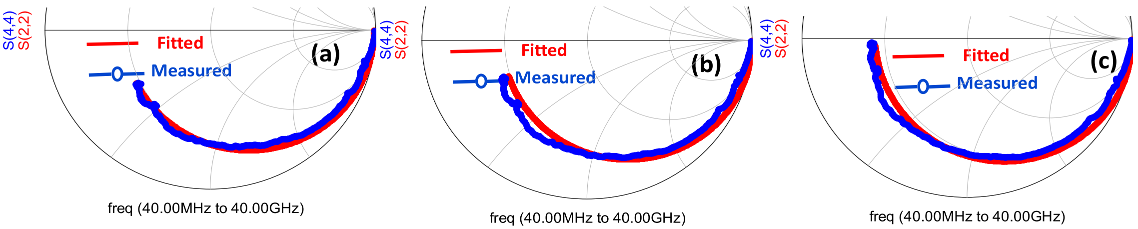

Fig. 7. Measured (blue line) and fitted (red line) S_{22} parameters from near dc to 40 GHz under a fixed dc bias (-23 V) for demonstrated devices A to C.

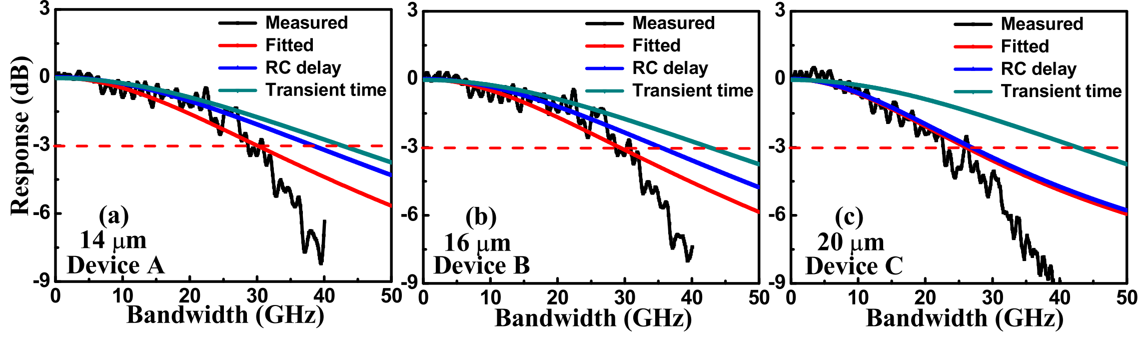

Fig. 8. Measured O-E, extracted RC-limited, transit time, and fitted O-E frequency responses for devices A to C.

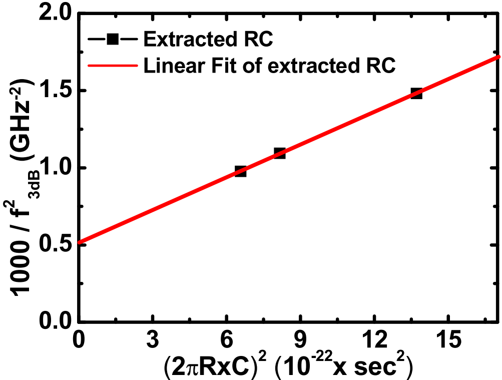

Fig. 9. Extracted $(1/f_{RC})^2$ versus measured $(10^3/f_{3dB}^2)$ for devices A to C.

carrier transit time. Fig. 9 depicts the values of $(1/f_{RC})^2$versus $(10^3/f_{3dB}^2)$ for the fabricated APDs (A to C). The internal carrier transit times in our devices are calculated using (1) and the fitted RC-limited and measured net O-E bandwidths for each device (see Figs. 7 and 8), from the intercepts along the y-axis in Fig. 9 [29]. The obtained f_t is approximately 44 GHz, which closely matches with the transit time limited bandwidth obtained using the equivalent circuit modeling technique 43 GHz, as seen in Fig. 6.

Fig. 10 depicts the photo-generated RF output saturation power measured with the heterodyne beating setup at a frequency of 30 GHz for these three devices at different bias voltage. The heterodyne-beating system consists of two free-running lasers that operate around the optical wavelength of 1.55 μm and have a 30 GHz (0.24 nm) spacing in their central wavelengths. For reference, the ideal relationship between the microwave power and the average photocurrent (pink line) with a 100% optical modulation depth under a 50 Ω load is plotted. We can clearly see that the value of the saturation photocurrent exhibited by all three devices is the same 11 mA for maximum output RF power under 0.95 V_{br}. For example, the measured responsivity of device A under a saturation output RF power of (-1.8 dBm), which corresponds to a high launched optical power of +8.8 dBm, is around 1.5 A/W. The traces measured at various V_{br} voltages also merge together as the output photocurrent rises, which can be explained by the shorter avalanche delay time and wider O-E bandwidth under high-power operation, as shown in Figs. 4 and 5. Compared with the high-power performance of APDs reported in our previous work [16], our new APD device A design, which has the same active mesa diameter of 24 μm exhibits the same saturation current around 11 mA at 0.95 V_{br} but at a higher heterodyne-beating frequency (30 vs. 20 GHz). Such a significant improvement in the saturation current-bandwidth product is mainly due to the improvement in the speed of the new APD, obtained by incorporating the dual M-layer design, without the need to downscale the active size of the device. As a result, this APD has the potential to further improve the S/N ratio when used in a high-speed coherent receiver, while requiring less optical LO power than a p-i-n PD. Table I shows the benchmark high-performance of these APDs with top- and back-side illuminated structures for 28 or 56 Gbaud transmission. We can clearly see that our device with its simple top-illuminated structure exhibits an excellent bandwidth-responsivity product and a record-high saturation current-bandwidth product among all reported high-speed APDs.

Authorized licensed use limited to: National Central University. Downloaded on March 27,2025 at 04:49:52 UTC from IEEE Xplore. Restrictions apply.

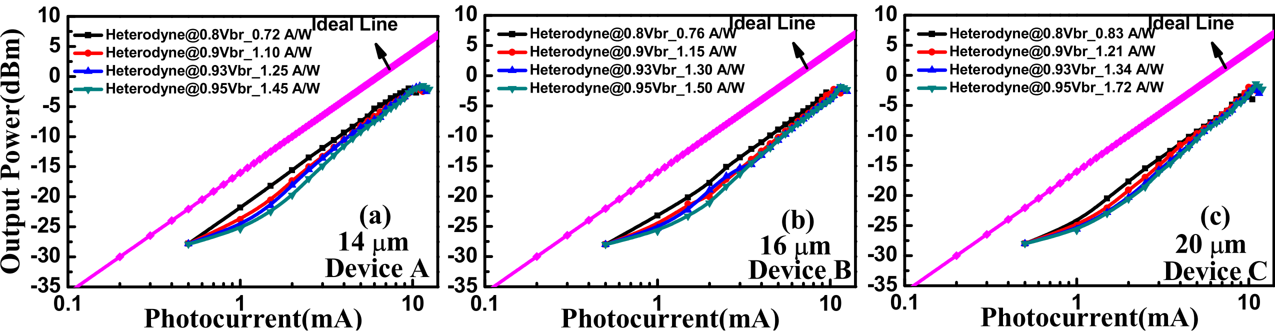

Fig. 10. Measured photo generated RF power versus photocurrent for devices A to C, at a frequency of 30 GHz for heterodyne beating under different V_{br}.

IV. Conclusion

In conclusion, our novel top-illuminated APD structure demonstrates excellent high-speed and high-power performance. We can fundamentally relax the trade-off between multiplication gain, speed, and dark current by downscaling the absorber and dual M-layer designs with a cascade avalanche process. Moreover, the p-side up and the special mesa structure with the composite charge layers can strongly confine the E-field at the center of the $In_{0.52}Al_{0.48}As$ based M-layer, greatly suppressing the edge breakdown phenomenon and resulting in a much lower dark current. Furthermore, this APD structure has the advantage of improved power performance due to better heat dissipation because the 2nd M-layer having the highest E-field region is buried at the bottom, close to the InP substrate. By optimizing the depletion width of the partially p-doped $In_{0.53}Ga_{0.47}As$ absorber and additional InP collector layers, the RC-delay time and internal transit time can be balanced. This allows our APDs to have a larger active diameter of 24 μm for greater optical alignment tolerance and better device heat sinking. At around 0.9 V_{br} bias voltage, this 24 μm active mesa diameter device can attain a high responsivity (2.23 A/W), low dark current ($\sim$200 nA), and a wide O-E bandwidth (30 GHz). During testing in a heterodyne beating system, a saturation output photocurrent (11 mA) at 30 GHz was observed. Our APD's excellent dynamic/static performance opens up new opportunities to further enhance the sensitivity of photoreceivers for coherent communications or 106 Gbit/sec PAM-4 applications.

References

[1] S. Kanazawa et al., "Flip-Chip interconnection lumped-electrode EADFB laser for 100-Gb/s/λ transmitter," *IEEE Photon. Technol. Lett.*, vol. 27, no. 16, pp. 1699–1701, Aug. 2015.
[2] Naseem et al., "Uni-Traveling carrier photodiodes with Type-II $GaAs_{0.5}Sb_{0.5}/In_{0.53}Ga_{0.47}As$ hybrid absorbers integrated with substrate lens in 400 Gbit/sec DR-4 system," in *Proc. Opt. Fiber Commun.*, Mar. 2020, pp. 1–3, Paper W4G.5.
[3] T. Yoshimatsu et al., "Suppression of space charge effect in MIC-PD using composite field structure," *Electron. Lett.*, vol. 46, no. 13, pp. 941–943, Jun. 2010.
[4] M. Nada, Y. Yamada, and H. Matsuzaki, "Responsivity-Bandwidth limit of avalanche photodiodes: Toward future ethernet systems," *IEEE J. Sel. Topics Quantum Electron.*, vol. 24, no. 2, Mar./Apr. 2018, Art. no. 3800811.
[5] M. Huang et al., "Germanium on silicon avalanche photodiode," *IEEE J. Sel. Topics Quantum Electron.*, vol. 24, no. 2, Mar./Apr. 2018, Art. no. 3800911.
[6] B. Shi et al., "106 Gb/s normal-incidence Ge/Si avalanche photodiode with high sensitivity," in *Proc. Opt. Fiber Commun. Conf. Exhibit.*, 2020, pp. 1–3.
[7] M. Nada, T. Yoshimatsu, F. Nakajima, K. Sano, and H. Matsuzaki, "A 42-GHz bandwidth avalanche photodiodes based on III-V compounds for 106-Gbit/s PAM4 applications," *J. Lightw. Technol.*, vol. 37, no. 2, pp. 260–265, Jan. 2019.
[8] M. Nada et al., "Inverted p-down design for high-speed photodetectors," *Photonics*, vol. 8, no. 2, 2021, Art. no. 39, doi: 10.3390/photonics8020039.
[9] E. Ishimura et al., "Degradation mode analysis on highly reliable guarding-free planar inalas avalanche photodiodes," *J. Lightw. Technol.*, vol. 25, no. 12, pp. 3686–3693, Dec. 2007.
[10] B. F. Levine et al., "A new planar InGaAs-InAIAs avalanche photodiode," *IEEE Photon. Tech. Lett.*, vol. 18, no. 18, pp. 1898–1900, Sep. 2006.
[11] C. Xie and J. Cheng, "Coherent optics for data center networks," in *Proc. IEEE Photon. Soc. Summer Topicals Meeting Ser.*, 2020, pp. 1–2.
[12] J. Cheng, C. Xie, Y. Chen, X. Chen, M. Tang, and S. Fu, "Comparison of coherent and IMDD transceivers for intra datacenter optical interconnects," in *Proc. Opt. Fiber Commun. Conf. Exhibit.*, Mar. 2019, pp. 1–3, Paper W1F.2.
[13] M. Anagnosti et al., "Record gain x bandwidth (6.1 THz) monolithically integrated SOA-UTC photoreceiver for 100-Gbit/s applications," *J. Lightw. Technol.*, vol. 33, no. 6, pp. 1186–1190, Mar. 2015.
[14] Z. Ahmad et al., "Avalanche photodiodes with dual multiplication layers and ultra-high responsivity-bandwidth products for FMCW lidar system applications," *IEEE J. Sel. Topics Quantum Electron.*, vol. 28, no. 2, Mar./Apr. 2022, Art. no. 3800709, doi: 10.1109/JSTQE.2021.3062637.
[15] P. Runge et al., "Waveguide integrated balanced photodetectors for coherent receivers," *IEEE J. Sel. Topics Quantum Electron.*, vol. 24, no. 2, Mar./Apr. 2018, Art. no. 6100307.
[16] Naseem et al., "Avalanche photodiodes with composite charge-layers for low dark current, high-speed, and high-power performance," *IEEE J. Sel. Topics Quantum Electron.*, vol. 28, no. 2, Mar./Apr. 2022, Art. no. 3801910, doi: 10.1109/JSTQE.2021.3111895.
[17] M. Nada, Y. Yamada, and H. Matsuzaki, "A high-linearity avalanche photodiodes with a dual-carrier injection structure," *IEEE Photon. Technol. Lett.*, vol. 29, no. 21, pp. 1828–1831, Nov. 2017.
[18] J. Wei, F. Xia, and S. R. Forrest, "A high-responsivity high-bandwidth asymmetric twin-waveguide coupled InGaAs-InP-InAlAs avalanche photodiode," *IEEE Photon. Technol. Lett.*, vol. 14, no. 11, pp. 1590–1592, Nov. 2002, doi: 10.1109/LPT.2002.803894.
[19] B. Wang et al., "64 Gb/s low-voltage waveguide SiGe avalanche photodiodes with distributed Bragg reflectors," *Photon. Res.*, vol. 8, no. 7, pp. 1118–1123, Jul. 2020.
[20] T. Okimoto et al., "106-Gb/s Waveguide AlInAs/GaInAs avalanche photodiode with Butt-joint coupling structure," in *Proc. Opt. Fiber Commun. Conf. Exhibit.*, 2022, pp. 01–03.
[21] T. Beckerwerth, R. Behrends, F. Ganzer, P. Runge, and M. Schell, "Linearity characteristics of avalanche photodiodes for InP based PICs," *IEEE J. Sel. Topics Quantum Electron.*, vol. 28, no. 2, Mar./Apr. 2022, Art. no. 3803408, doi: 10.1109/JSTQE.2021.3127853.
[22] J.-S. Choe et al., "Optimization of spot-size converter for low polarization dependent loss of waveguide photodetector," *Opt. Exp.*, vol. 21, no. 25, pp. 30175–30182, Dec. 2013.

Authorized licensed use limited to: National Central University. Downloaded on March 27,2025 at 04:49:52 UTC from IEEE Xplore. Restrictions apply.

[23] J. Y. Huh, S.-K. Kang, J. H. Lee, J. K. Lee, and S. M. Kim, "Highly alignment tolerant and high-sensitivity 100Gb/s (4 × 25Gb/s) APD-ROSA with a thin-film filter-based de-multiplexer," *Opt. Exp.*, vol. 24, no. 24, pp. 27104–27114, Nov. 2016.
[24] Albis Optoelectronics AG, Moosstrasse 2a, 8803 Rueschlikon, Switzerland. (Product: APD20D1 on Submount).
[25] J.-M. Wun, C.-H. Lai, N.-W. Chen, J. E. Bowers, and J.-W. Shi, "Flip-Chip bonding packaged THz photodiode with broadband high-power performance," *IEEE Photon. Technol. Lett.*, vol. 26, no. 24, pp. 2462–2464, Dec. 2014.
[26] Naseem et al., "Avalanche photodiodes with dual multiplication layers for high-speed and wide dynamic range performances," *Photonics*, vol. 8, no. 4, Mar. 2021, Art. no. 98.
[27] N. Li et al., "High-saturation-current InGaAs/InAlAs charge-compensated uni-traveling-carrier photodiode," *Phys. Statist. Sol. (a)*, vol. 201, no. 13, pp. 3037–3041, Aug. 2004.
[28] Y. L. Goh, J. S. Ng, C. H. Tan, W. K. Ng, and J. P. R. David, "Excess noise measurement in $in_{0.53}Ga_{0.47}As$," *IEEE Photon. Technol. Lett.*, vol. 17, no. 11, pp. 2412–2414, Nov. 2005.
[29] Naseem et al., "The enhancement in speed and responsivity of uni-traveling carrier photodiodes with $GaAs_{0.5}Sb_{0.5}/In_{0.53}Ga_{0.47}As$ type-II hybrid absorbers," *Opt. Exp.*, vol. 27, no. 11, pp. 15495–15504, May 2019.
[30] J.-W. Shi, K.-L. Chi, C.-Y. Li, and J.-M. Wun, "Dynamic analysis of high-efficiency InP based photodiode for 40 Gbit/sec optical interconnect across a wide optical window (0.85 to 1.55 μm)," *J. Lightw. Technol.*, vol. 33, no. 4, pp. 921–927, Feb. 2015.
[31] Albis Optoelectronics AG, Moosstrasse 2a, 8803 Rueschlikon, Switzerland. (Product: APD20E1 28 Gbd Top-side Illuminated APD).
[32] H.-Y. Zhao et al., "High-Speed avalanche photodiodes with wide dynamic range performance," *J. Lightw. Technol.*, vol. 37, no. 23, pp. 5945–5952, Dec. 2019.
[33] G. S. Kinsey, J. C. Campbell, and A. G. Dentai, "Waveguide avalanche photodiode operating at 1.55 µm with a gain-bandwidth product of 320 GHz," *IEEE Photon. Tech. Lett.*, vol. 13, no. 8, pp. 842–844, Aug. 2001.

Naseem was born in the Punjab, India in 1991. He received the M.Tech. degree from the Department of Nanotechnology, Jamia Millia Islamia, New Delhi, India. He is currently working toward the Ph.D. degree with the Department of Electrical Engineering, National Central University, Taoyuan, Taiwan. His research interests include high-speed photodiodes and avalanche photodiodes for optical receivers.

Po-Shun Wang was born in Kaohsiung, Taiwan on June 02, 1998. He is currently working toward the master's degree with the Department of Electrical Engineering, National Central University, Taoyuan, Taiwan. His research interests include single-photon avalanche diodes and avalanche photodiodes.

Zohauddin Ahmad was born in Bihar, India in 1989. He received the graduation degree from the Department of Nanoscience and Nanotechnology, Jamia Millia Islamia, New Delhi, India. He is currently working toward the Ph.D. degree from the Department of Electrical Engineering, National Central University, Taoyuan, Taiwan. His research interests include high-speed modulator-based lasers, FMCW-Lidar, and photonics integrated circuits.

Syed Hasan Parvez is from Lucknow, India. He received the graduation and master's degree in nanotechnology from the Centre for Nanoscience and Nanotechnology, Jamia Millia Islamia, New Delhi, India. He is currently working toward the Ph.D. degree with the Department of Electrical Engineering, National Central University, Taoyuan, Taiwan. His research interests include high speed photodiodes, APDs (Avalanche Photodiodes) for optical receivers, and measurements.

Sean Yang received the B.S. degree in electrical engineering from National Taiwan Ocean University, Keelung, Taiwan, in 2006. He was with E Ink Holdings Inc., as a Photo Engineer, from 2006 to 2017. He is currently with Source Photonics Inc., as an Engineer of Advanced Tools.

H.-S. Chen received the Ph.D. degree from the Graduate Institute of Photonics and Optoelectronics, National Taiwan University, Taipei, Taiwan, in 2006. Since June 2007, he has been a Postdoctoral Research Fellow with the Institute of Physics, Academia Sinica. From 2011 to 2013, he was with the Institute of Photonics and Optoelectronics, National Taiwan University, as a Postdoctoral Fellow. His research interests include surface plasmon, near field optics, ultrafast lasers, nanorod array LEDs, and optical sensors. In 2014, he joined Source Photonics Inc., as Manager of Advanced Process Development.

Hsiang-Szu Chang received the M.S. and Ph.D. degrees from the Solid-state Optics Lab, Department of Physics, National Central University, Taoyuan, Taiwan, in 2002 and 2009, respectively. He is currently with Source Photonics Inc., as Senior Engineer of Product Development, OE devices.

Jack Jia-Sheng Huang received the B.S. degree in physics from National Taiwan University, Taipei, Taiwan in 1992, and the M.S. and Ph.D. degrees in materials science from UCLA in 1996 and 1997, respectively. He has more than 90 publications in international journals and conferences in the areas of optoelectronics and ICs. He holds six U.S. patents and one U.K. patent. In 1997, he was the recipient of the Outstanding Ph.D. Award and Dissertation Year Fellowship Award from the Henry Samueli School of Engineering, UCLA. He is currently a Senior R&D Scientist/Manager at Source Photonics, working on Advanced Photonics Devices, including 100G DML, 40G CWDM DFB, 10G DFB, and 10G FP lasers and 10G and 25G APD photodetectors. His R&D projects also involve device reliability physics and device characterization. From 2000 to 2015, he was a Wafer Fab R&D/Operations Manager at Emcore, working on device design/process/characterization, reliability, electrostatic discharge (ESD) and failure analysis of analog BH lasers and digital ridge lasers for cooled and uncooled applications. From 1997 to 2000, he was a Member of Technical Staff at Lucent Technologies, Bell Labs, Orlando, FL, working on electromigration, stress migration and failure analysis of 0.3, 0.25, 0.2 and 0.16mm ASIC and FPGA devices using CMOS technology. From 1992 to 1993, he was a Research Assistant with the Institute of Atomic and Molecular Sciences, Academia Sinica, Taiwan, studying the surface physics of gallium ion beams in an ultra-high vacuum.

Jin-Wei Shi (Senior Member, IEEE) was born in Kaohsiung, Taiwan on January 22, 1976. In 2003, he joined the Department of Electrical Engineering, National Central University, Taoyuan, Taiwan, where he was with the position of Professor since 2011. From 2011 to 2012 and 2016 to 2017, he joined the ECE Department of UCSB as a Visiting Professor. He has authored or coauthored more than four book chapters, 150 journal papers, 200 conference papers and holds 30 patents. His research interests include ultra-high speed/power photodetectors, electro-absorption modulators, THz photonic transmitters, and VCSELs. In 2010, he was the recipient of the Da-You Wu Memorial Award.

Authorized licensed use limited to: National Central University. Downloaded on March 27,2025 at 04:49:52 UTC from IEEE Xplore. Restrictions apply.